electronics

MDPI

Article

Thermoelectric-Powered Remote Sensor for Frost Detection

Martim Lima de Aguiar [1,2], Pedro Dinis Gaspar [1,2] and Pedro Dinho da Silva [1,2,*]

[1] Department of Electromechanical Engineering, Faculty of Engineering, University of Beira Interior, Rua Marquês d'Ávila e Bolama, 6201-001 Covilhã, Portugal; martim.aguiar@ubi.pt (M.L.d.A.); dinis@ubi.pt (P.D.G.)
[2] C-MAST—Center for Mechanical and Aerospace Science and Technologies, 6201-001 Covilhã, Portugal
* Correspondence: dinho@ubi.pt

Abstract: This article proposes the use of a thermoelectric system as an energy-harvesting device for use in industrial refrigeration units. The energy generated by the device in this study can be used for remote, low-power applications, such as frost detection sensors. The accumulation of frost on the surfaces of evaporators causes inefficiency in the operation of refrigeration units by reducing the heat exchange rate. To revert this condition, the evaporator must be defrosted periodically. The proposed energy-autonomous sensors can be localized in key places to minimize not only the number of defrosting operations but also their duration. These sensors can transmit data wirelessly so that the control systems can better determine the ideal time to perform defrosting operations. This device eliminates the need for complex cable routing in long systems, where these components are often located far apart or in hard-to-reach places. The outcomes of this research not only offer solutions to a prevailing issue in refrigeration units but also aid in formulating strategies for optimally placing ice formation detection sensors. Additionally, these findings may boost overall refrigeration efficiency while cutting down on installation and maintenance costs.

Keywords: energy harvesting; thermoelectric devices; remote sensing; defrosting operations; refrigeration systems; energy efficiency

check for updates

Citation: Aguiar, M.L.d.; Gaspar, P.D.; da Silva, P.D. Thermoelectric-Powered Remote Sensor for Frost Detection. *Electronics* **2024**, *13*, 2683. https://doi.org/10.3390/electronics13142683

Academic Editor: Inhee Lee

Received: 6 June 2024
Revised: 1 July 2024
Accepted: 6 July 2024
Published: 9 July 2024

Copyright: © 2024 by the authors. Licensee MDPI, Basel, Switzerland. This article is an open access article distributed under the terms and conditions of the Creative Commons Attribution (CC BY) license (https://creativecommons.org/licenses/by/4.0/).

1. Introduction

Refrigeration systems are fundamental to various industrial processes, from food preservation to pharmaceutical storage. However, the efficiency of these systems can be severely decreased by the accumulation of frost on evaporator surfaces [1]. In the food sector, namely in light commercial systems, heat exchangers (HXs) with a large area-to-volume ratio are particularly susceptible to frost accumulation on fin surfaces when operating under subfreezing temperature conditions [1–3]. The presence of frost acts as a thermal barrier, reducing thermal performance and restricting heat transfer between air and the refrigerant [4,5], while also increasing energy consumption [6–8].

The design of HXs must account for frost formation to avoid operational issues. Without appropriate design and defrosting methods, frost buildup can restrict or, in worst-case scenarios, block airflow between fins. This leads to increased energy consumption, lower performance, degradation of refrigeration conditions, decreased product safety and quality, and potential system damage [9,10]. Figure 1 shows the frost formation process on the intake side of a HX. The images illustrate the sequential stages of frost development, starting from minimal accumulation (a), progressing to initial frost formation in localized regions (b), and culminating in complete blockage of the HX surface (c). This figure displays the irregular and unpredictable progressive nature of frost buildup and its potential to decrease thermal performance, emphasizing the need for effective frost management strategies in HX design and operation.

In previous studies [9,11,12], sensor technology has been demonstrated as an effective method for frost detection and as a tool for controlling demand defrosting operations.

Traditional frost detection methods, which rely on prediction based on ambient conditions or on the monitoring of system working parameters, often prove irregular and unreliable due to the unpredictable nature of frost formation. This irregularity necessitates more accurate detection techniques. Various sensors, such as photoelectric [13], capacitive [14], piezoelectric, optical fiber [15], and resistive sensors [12], have been investigated and found to significantly improve the accuracy of frost detection and the efficiency of defrosting operations compared to conventional time-based methods. Ge et al. [13] studied a Tube Encircled Photoelectric Sensor (TEPS), and its performance was compared to that of the default timed defrosting method in the refrigeration system. The study demonstrated that demand defrosting using a sensor significantly reduced the frequency of defrosting operations. Specifically, as shown in Figure 2, over a 24 h period, the sensor-controlled defrosts resulted in only eight defrosting operations, compared to the 30 defrosts scheduled for the worst-case scenario based on timed defrosts.

Figure 1. Stages of frost formation on the intake side of a HX, with minimal accumulation (**a**), initial frost formation (**b**), and complete blockage (**c**) [9].

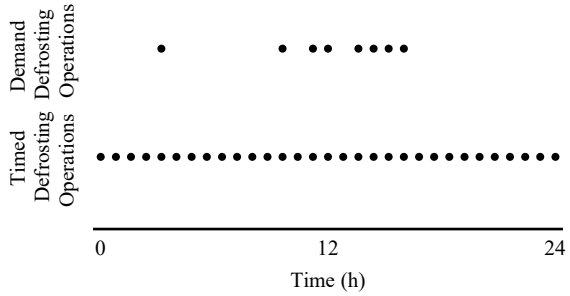

Figure 2. Comparison between timed and demand defrosting using the TEPS sensor. The dots indicate defrosting operations occurring only when necessary under the demand defrosting method and periodically for the timed defrosting operations [12].

These eight defrosting operations were irregularly distributed and triggered based on the amount of frost accumulated on the HX. This demonstrates the potential of demand defrosting using sensors to enhance energy efficiency and minimize additional thermal loads from unnecessary defrosting operations. At the same time, it prevents excessive frost accumulation, which can adversely affect overall system performance, as previously discussed.

This way, modern refrigeration systems integrating Internet of Things (IoT) technologies can enhance operational efficiency and accuracy. IoT systems contain Wireless Sensor Networks (WSNs) of interconnected devices that communicate and share data wirelessly. WSNs are components of the IoT, consisting of spatially distributed sensors that monitor environmental conditions and transmit data to a central system. These sensors can provide real-time monitoring and control [16]. In the context of mitigating the problem of frost

formation, IoT sensor networks can monitor refrigeration systems' working parameters, which can be used as data to feed decision support tools for demand defrosting operations, such as demand defrost algorithms [12], digital twinning, deep learning, and artificial intelligence [17]

Implementing a sensor within a HX presents several complexities, particularly in compact or remote HX applications. The issue of the availability of energy to power the sensing module and issues related to cable management and the integration of the sensor into the existing system without causing disruption make a wireless sensing module an interesting approach. Sensors such as the resistive sensor developed in previous studies [12] have very low energy requirements due to their overall simplicity and low acquisition rate, making them suitable for integration into low-power energy-autonomous wireless sensing modules.

Given the wide temperature gradients within refrigeration systems, a thermoelectric system presents an attractive solution as a power generation unit for wireless sensing modules. Thermoelectric generators (TEGs) use the Seebeck effect to convert heat flow, which is driven by temperature gradients, into electrical energy. By tapping into these temperature gradients, thermoelectric systems can provide a sustainable and reliable power source for low-power applications [18], eliminating the need for repeated exchange of batteries or connection to external power supplies or extensive wiring.

In recent years, there has been a growing interest in the usage of thermoelectric systems for powering low-power devices. Research by Alvarez-Quintana [19] demonstrates the feasibility of using TEG modules to harvest electrical power from condenser heat in refrigeration systems, reaching close to 20 mW with a single commercial cell.

In another study, Attar et al. [20] designed and manufactured a HX with 16 TEG cells, implemented into refrigeration systems for de-superheating of refrigerants after the compression phase, demonstrating that the harvested energy could be used to power auxiliary systems, attaining power generations of 3 W to 12 W (average of 0.2 W to 0.7 W per cell), depending on the usage of a fan to increase heat transfer.

Due to a low electrical power-to-heat transfer ratio, implementation of TEGs requires careful study. Using a TEG generator between the evaporator and condenser would yield a higher temperature gradient, and therefore a higher electrical power generation. Nonetheless, this placement would be very inefficient, as it would introduce a significant thermal load, outweighing the benefits of a demand defrost system. Instead, these systems should be integrated where heat exchange is already intended, such as between the evaporator and intake air, between the condenser and refrigerating air, or in the liquid-to-suction line used by the HX to superheat the gas and subcool the liquid, such as the in application in [20]. This approach ensures that the TEG system generates electrical power without adding undesired thermal loads.

The current study aims to evaluate the feasibility of using thermoelectric energy harvesting to power frost detection sensors in refrigeration systems. An experimental setup was developed to simulate the conditions found in refrigeration units, with a HX module containing four Peltier cells. One side of the module was cooled, and the other was heated, representing a temperature gradient and an associated heat transfer through the module.

The primary objective was to measure the power output of the TEG HX and assess its potential for remote sensor applications. The ability to convert heat flow into electrical energy for powering frost detection sensors presents a dual potential for energy efficiency. On the one hand, the sensor contributes to accurate frost detection and precise defrosting operations. On the other hand, the power for this system could be obtained from the dissipation of waste heat, such as in the condenser, by extracting energy from a temperature gradient that the refrigeration system creates to discard the heat. If waste heat is not available, a small amount of energy can be obtained from a location where heat flow is already desired, at the expense of introducing a small heat resistance to the HX. In such cases, the system should be designed to minimize disruption to normal system parameters,

either by having a small footprint or by being placed in a way that its thermal resistance does not significantly impact the normal heat exchange process.

2. Materials and Methods

The experimental setup consists of a simulated HX such as those in the liquid-to-suction line found in refrigeration systems, used to superheat the gas and subcool the liquid. In this experiment, a liquid-to-liquid HX configuration was utilized. The working fluid circuit and its components are represented in Figure 3. The cold circuit (blue dashed line) consists of a chiller, reservoir (D_c), intake ($T_{c,\,in}$) and outlet ($T_{c,\,out}$) temperature sensors, pump (P_c), and flow meter (V_c). Liberated heat from the hot circuit (red dashed line) is transferred through the TEG HX and absorbed by the cold circuit. The hot circuit includes an air tunnel with another HX and air temperature control, intake ($T_{h,\,in}$) and outlet ($T_{h,\,out}$) temperature sensors, pump (P_h), and flow meter (V_h).

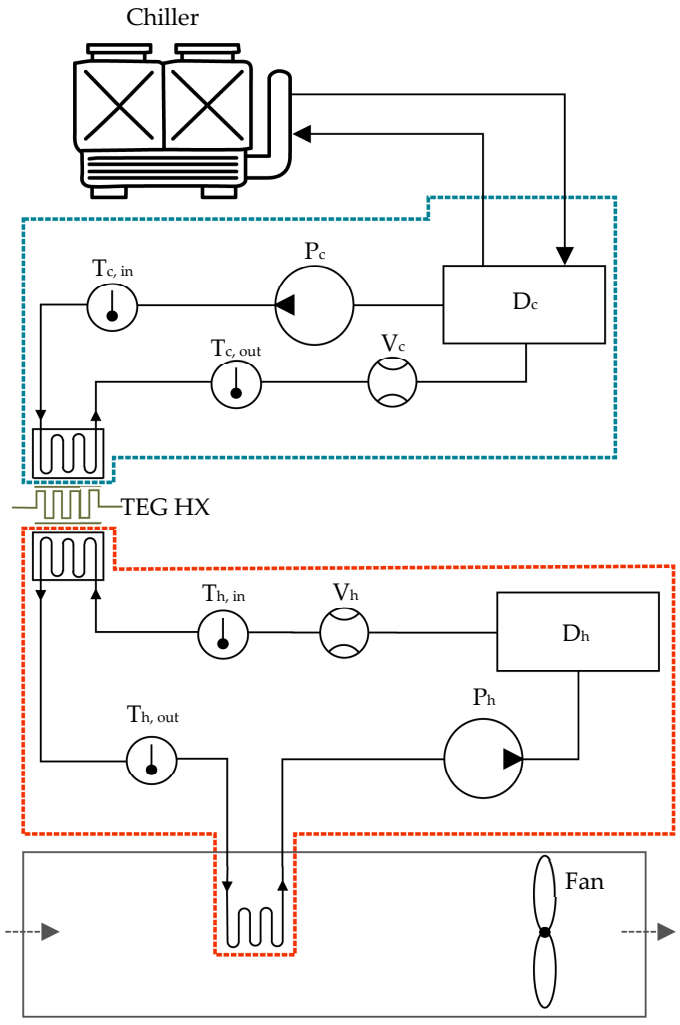

Figure 3. Schematic of the experimental setup showing all components of the cold and hot circuits, installed sensors, and the TEG HX.

The cold circuit is designed to absorb heat from the hot circuit and is comprised of the following components:

- Chiller: Provides cooling to maintain a constant heat transfer in the TEG HX.
- Reservoir: Dampens temperature fluctuations and holds cold working fluid.
- Intake and outlet temperature sensors: Monitor the temperature of the cold working fluid entering and exiting the HX, with an accuracy of ± 0.5 K.

- Pump: Circulates the cold working fluid through the cold circuit.
- Flow meter: Measures the flow rate of the cold working fluid, with an accuracy of ±5%.

The hot circuit transfers heat to the cold circuit through the TEG HX and includes the following components:

- Air tunnel: Contains another HX that absorbs heat from the air. The air temperature within the tunnel can be controlled to simulate various conditions.
- Reservoir: Dampens temperature fluctuations and holds hot working fluid.
- Intake and outlet temperature sensors: Measure temperatures of the hot working fluid entering and exiting the TEG HX, with an accuracy of ±0.5 K.
- Pump: Circulates the hot working fluid through the hot circuit.
- Flow meter: Measures the flow rate of the hot working fluid, with an accuracy of ±5%.

2.1. Thermoelectric Generator Heat Exchanger (TEG HX)

The TEG HX is the focus of this study and the main component of the experimental setup. It generates electrical energy through the Seebeck effect using four thermoelectric Peltier modules. Figure 4 illustrates this component, with Figure 4a providing an exploded view and Figure 4b showing a rendering of the TEG HX.

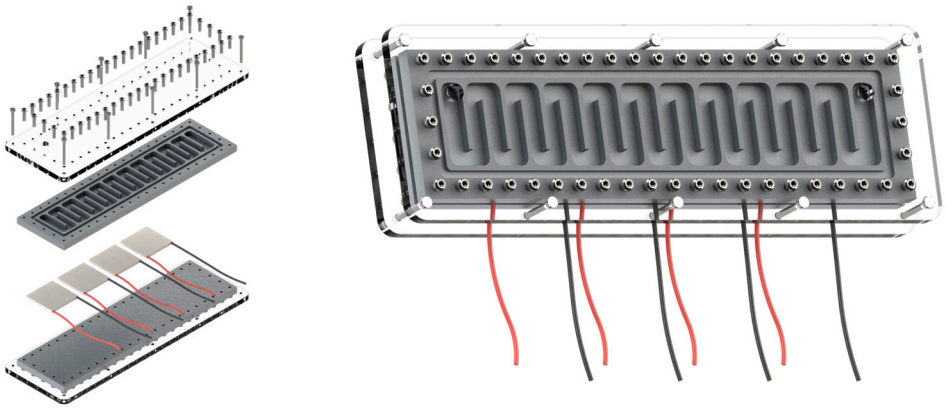

(**a**) (**b**)

Figure 4. Exploded (**a**) and assembled (**b**) view of the TEG HX, showing the four Peltier cells, machined aluminum plates, lids, and fixtures.

The assembly consists of four Peltier cells, two aluminum plates in which channels for the working fluid were CNC-machined to maximize the heat exchange surface in both cold and hot circuits, corresponding acrylic lids, and fixtures. To enhance thermal conductivity, thermal paste was applied between the TEG and the aluminum plates on both sides.

2.2. Circuit, Measurements, and Data Acquisition

The four Peltier cells were connected in series, as depicted in the schematic in Figure 5. This series configuration was further connected to a resistor, with a microcontroller whose ADC is used to measure the voltage drop across the resistor terminals with an accuracy of ±9.8 mV. For each test, a series of different resistors ranging from 0.78 Ω up to 14,861.44 Ω were tested to determine the maximum TEG power output. The resistance values for each resistor tested were measured, including wiring resistance, with an accuracy of ±(0.05% of the reading + 1 LSD).

The voltage drop across the resistor R is measured using a 10 bit Analog-to-Digital Converter (ADC). Given the known resistance value for each resistor tested, the current and thus the power can be calculated from these measurements. The following steps summarize the measurement process.

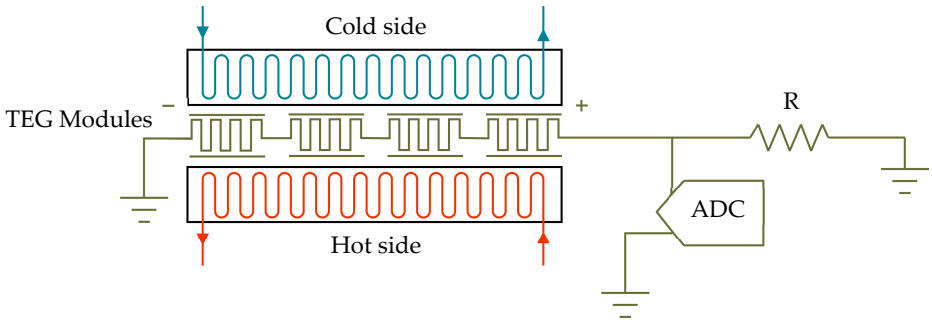

Figure 5. Schematic diagram of the TEG HX electrical configuration and data acquisition setup.

2.3. Electric Power Generation

The *ADC* measures the voltage drop across the resistor, returning a value from 0 to 1023, which corresponds to a voltage of between 0 V and 5 V, respectively. To calculate the voltage, this measurement is introduced into Equation (1):

$$V = \frac{ADC \times 5}{1023} \tag{1}$$

where V is the measured voltage, and ADC is the value returned by the ADC. From here, and knowing the value of R, the power can be calculated by replacing the known value of R and V in Equation (2):

$$P_{elec} = \frac{V^2}{R} \tag{2}$$

This results in Equation (3):

$$P_{elec} = \frac{\left(\frac{ADC \times 5}{1023}\right)^2}{R} \tag{3}$$

This is directly calculated in the acquisition system, returning the electrical power generated (P_{elec}).

2.4. Heat Transfer

The heat flow ($\dot{Q}$) for both the cold and hot sides can be calculated using Equations (4) and (6): For the cold side,

$$\dot{Q}_c = \dot{V}_c \times \rho_c \times C_{p,\,c} \times \Delta T_c \tag{4}$$

ΔT_c can be obtained from Equation (5):

$$\Delta T_c = T_{c,\ out} - T_{c,\,in} \tag{5}$$

For the hot side,

$$\dot{Q}_h = \dot{V}_h \times \rho_h \times C_{p,\,h} \times \Delta T_h \tag{6}$$

ΔT_h can be obtained from Equation (7):

$$\Delta T_h = T_{h,\ out} - T_{h,\,in} \tag{7}$$

where

$\dot{Q}_c$ and $\dot{Q}_h$ are the heat flows at the cold and hot sides respectively, in [W];
$\dot{V}_c$ and $\dot{V}_h$ are the volumetric flow rates for the cold and hot working fluids, respectively, in $\left[\mathrm{cm}^3/\mathrm{s}\right]$;
ρ_c and ρ_h are the densities for the cold and hot working fluids, respectively, in $\left[\mathrm{g}/\mathrm{cm}^3\right]$;

$C_{p,\,c}$ and $C_{p,\,h}$ are the specific heat capacities for the cold and hot working fluids, respectively, in [J/g·K];
ΔT_c and ΔT_h are the difference between inlet and outlet temperatures for the cold side and the hot side, respectively, in [K];
$T_{h,\,in}$, $T_{h,\,out}$, $T_{c,\,in}$, and $T_{c,\,out}$ are the working fluid temperatures, measured at the inlet and outlet for the hot and cold sides, respectively, in [K].

The working fluid used in both the hot and cold circuits is a mixture of water and glycol (40% by volume). The average temperature for all the tests is 271.1 K for the cold side and 299.0 K for the hot side. At these temperatures, and for this water–glycol mixture, the density at the average cold side temperature is 1.068 g/cm^3, and at the average hot side, the temperature is 1.053 g/cm^3. The specific heat capacities at these temperatures are 3.630 J/g·K for the cold side and 3.717 J/g·K for the hot side. With this in mind, $\dot{Q}_c$ and $\dot{Q}_h$ are calculated using Equations (8) and (9), respectively:

$$\dot{Q}_c = \dot{V}_c \times 1.068 \times 3.630 \times (T_{c,\ out} - T_{c,\,in}) \tag{8}$$

and

$$\dot{Q}_h = \dot{V}_h \times 1.053 \times 3.717 \times (T_{h,\ out} - T_{h,\,in}) \tag{9}$$

2.5. Energy Requirements

The feasibility of powering an acquisition system with the generated power must consider the system energy requirements. The acquisition system comprises an ESP32 microcontroller and a voltage divider with a resistive sensor. According to the ESP32 Datasheet [21], power is given in mA, with the knowledge that the working voltage is 3.3 V. Applying Equation (10) to the datasheet values, power is given in mW.

$$P = V \times I \tag{10}$$

The electric power consumption in mW is presented in Table 1 for the different modes, together with the time required to execute each objective.

Table 1. ESP32 power requirements in different modes, adapted from [21].

Mode	Objective	Execution Time	Power Consumption
Active	Data transmission	<1 s	330 mW to 792 mW
Modem-sleep	Execute sensor readings	50 ms	66 mW to 224 mW
Light-sleep	Wait for next frost measurement	-	2.64 mW

The system's energy usage per operation is given by Equation (11):

$$E = P \times \Delta t \tag{11}$$

where
E is the required energy for that operation, in [mJ];
P is the required power for that mode, in [mW];
Δt is the operation execution time, in [s].

Based on frost formation studies [13], it is reasonable to assume that in worst-case scenarios, defrosting is required once per hour. Therefore, to implement an effective frost-measuring sensor, the minimum requirement would be to transmit data at least once per hour. If a measurement frequency of one reading every 10 min is applied, the evolution of frost formation could also be obtained, which could help in assessing frost formation conditions and predict future defrosting needs.

This way, within each hour (3600 s), there would be 6 measurements, taking a total of 0.3 s, and one transmission lasting 1.0 s. This leaves a sleep time of 3598.7 s. Applying these values to Equation (12), we obtain the result in Equation (13)

$$E = P_{measure} \times \Delta t_{measure} + P_{transmission} \times \Delta t_{transmission} + P_{sleep} \times \Delta t_{sleep} \quad (12)$$

This results in an hourly energy demand of

$$E = 224 \times 0.3 + 792 \times 1 + 2.64 \times 3598.7 = 10,359.8 \text{ mJ} = 10.4 \text{ J} \quad (13)$$

In conclusion, the absolute minimum energy requirement for the presented sensing system is calculated to be 10.4 J per hour of operation. This estimation seeks to establish a value that the TEG must surpass so that that the system can operate effectively under the specified conditions, accounting for the necessary data transmission, sensor readings, and sleep periods. Because the power requirements will vary over time—with long periods of low power usage during sleep and peaks in power consumption during transmission—an electrical energy storage system, such as a small battery, will be needed as a buffer. This storage system will accumulate energy during sleep periods to cover the excess energy consumption during reading and transmission.

However, potential inefficiencies should also be accounted for. Small IOT devices with an ability to generate enough power to be self-sustainable such as the one developed by Kuang et al. [22] should consider generating approximately 20–30% more energy than the calculated requirements. This additional energy accounts for inefficiencies in the power management system and energy losses during rectification and storage, safeguarding reliable operation and sustainability. To ensure reliable operation by compensating for potential energy losses in accumulation and transmission, a 30% margin was selected. This adjustment increases the final power requirement to 13.5 J, which will be the value used for all subsequent calculations and analyses.

3. Results

The experimental tests conducted comprised three distinct 30 min intervals, each executed within a stable regime, after the system reached thermal equilibrium and operated in a non-transitional state. During this period, inlet and outlet working fluid temperatures ($T_{h,\,in}$, $T_{h,\,out}$, $T_{c,\,in}$, and $T_{c,\,out}$), volumetric flow in the hot and cold sides (V_h and V_c), and power generated in the TEG (P_{elec}) were measured and registered at 3 s intervals for both the cold and hot sides of the TEG HX.

3.1. Working Fluid Temperatures

Figure 6 shows the inlet and outlet temperatures of the working fluids across all the three tests. The inlet temperature on the cold side of the TEG HX remained constant at an average of 269.5 K, with a standard deviation of 0.17 K. Conversely, the inlet temperature on the hot side was modulated as the variable parameter across the tests. This parameter underwent incremental adjustments of 12.7 K and 14.6 K, respectively. Consequently, these adjustments yielded average temperature differentials between the hot and cold sides of the TEG HX ($\Delta T_{h-c\ AVG}$) of 16.3 K, 27.6 K, and 39.8 K, with standard deviations of 0.28 K, 0.23 K, and 0.48 K, respectively, for the three tests. The different experiments aim to simulate conditions like those found in different regions of refrigeration systems, as discussed in Section 2.

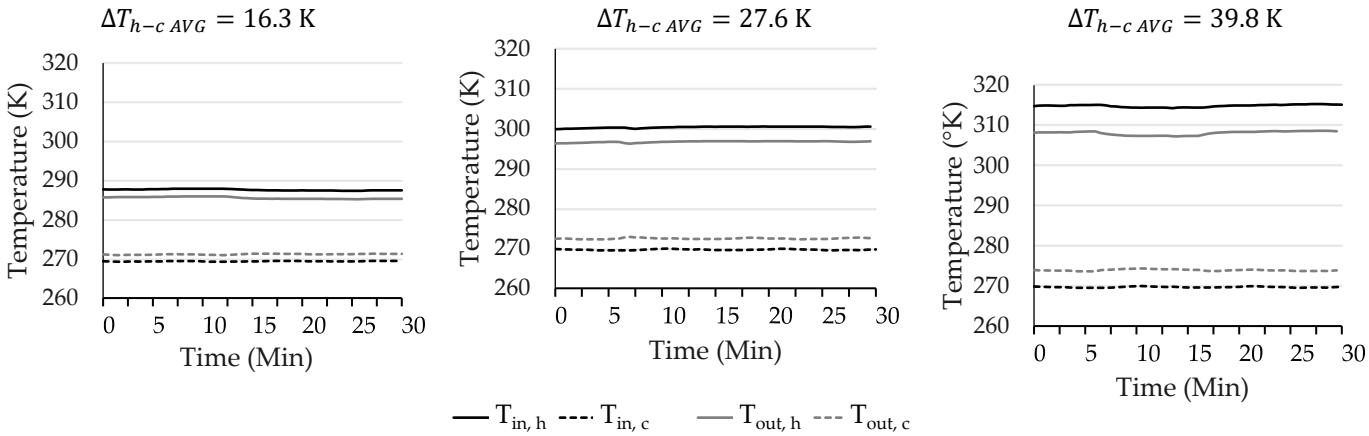

Figure 6. TEG HX inlet and outlet temperatures for the cold and hot sides under the three studied conditions.

Figure 6 shows the temperature profiles recorded throughout the three tests.

The maintenance of the cold side temperature and the incremental adjustments applied to the hot side temperature between tests can be seen. Though overall stability is observable, a slight temperature increase is discernible during the third test. During this test, a small increase of 0.37 K was measured from the start to the end of the test. Along with slight temperature fluctuations, this is reflected in the higher standard deviation values for Test 3 presented in Table 2. Nonetheless, the standard deviations remain within acceptable limits. These irregularities are mostly attributed to the hysteresis temperature control method of the thermostat on the hot side.

Table 2. Average temperature differences between inlet and outlet and respective standard deviation for hot and cold sides across the three tests.

	ΔT_h [K]	$\sigma_{\Delta T_h}$ [K]	ΔT_c [K]	$\sigma_{\Delta T_c}$ [K]
Test 1 : $\Delta T_{h-c\ AVG}$ = 16.3 K	−2.07	0.10	1.78	0.08
Test 2 : $\Delta T_{h-c\ AVG}$ = 27.6 K	−3.65	0.06	3.04	0.09
Test 3 : $\Delta T_{h-c\ AVG}$ = 39.8 K	−6.77	0.21	4.27	0.15

ΔT_c is consistently lower than ΔT_h; this difference gradually increases from Test 1 to Test 3, primarily due to varying flow rates on the hot and cold sides during the tests.

3.2. Flow Rates

The volumetric flow rate remained mostly constant throughout the data acquisition process for each of the tests; however, significant variations between tests are observable in Figure 7.

Notably, there was a descending trend in the average volumetric flow rate on the hot side, although it remained relatively stable during testing, as confirmed by the standard deviation values presented in Table 3.

Conversely, the average volumetric flow rates on the cold side remained more stable during the three tests. A slight descending trend was observed in Test 3 due to a slow increase in working fluid pressure in the pump outlet. Nonetheless, volumetric flow rates remained relatively stable during testing, as confirmed by the standard deviation values.

The significant variations between tests stemmed from a decrease in the section of the flow limiter as the working fluid temperature increased. This was particularly observable in the transition zones between tests. The low flow rate was intentional, to increase the temperature differential across the TEG HX. A low value of ΔT_c and ΔT_h

can approach the temperature sensor's margin of error, resulting in a relatively large measurement uncertainty.

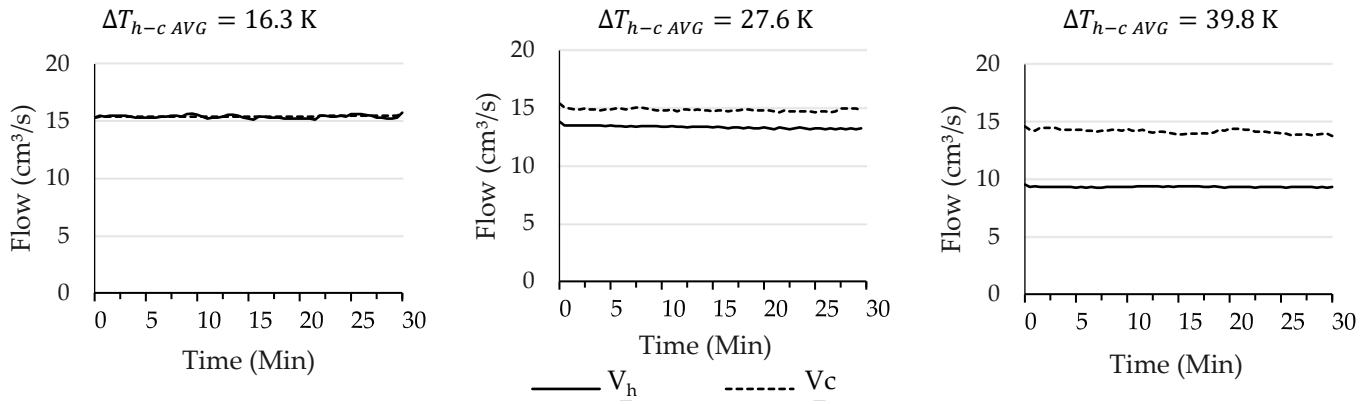

Figure 7. TEG HX flow for the cold and hot sides under the three studied conditions.

Table 3. Average flow rates and respective standard deviation for hot and cold sides across the three tests.

	$\mathbf{V_h}$ [cm³/s]	σ_{Vh} [cm³/s]	$\mathbf{V_c}$ [cm³/s]	σ_{Vc} [cm³/s]
Test 1 : $\Delta T_{h-c\ AVG}$ = 16.3 K	15.4	0.35	15.4	0.39
Test 2 : $\Delta T_{h-c\ AVG}$ = 27.6 K	13.4	0.28	14.8	0.34
Test 3 : $\Delta T_{h-c\ AVG}$ = 39.8 K	9.3	0.23	14.0	0.47

3.3. Heat Flow

Utilizing the volumetric flow rates ($\dot{V}_c$ and $\dot{V}_h$), along with the calculated differences between measured inlet and outlet temperatures (ΔT_c and ΔT_h), the specific heat capacity ($C_{p,\,c}$ and $C_{p,\,h}$), and density of the hot and cold working fluid discussed in the preceding section, the heat flow ($\dot{Q}_c$ and $\dot{Q}_h$) was calculated. For this, Equations (8) and (9) were used for determining the heat flow on the cold and hot sides, respectively. The resulting plots depicting these calculations are illustrated in Figure 8.

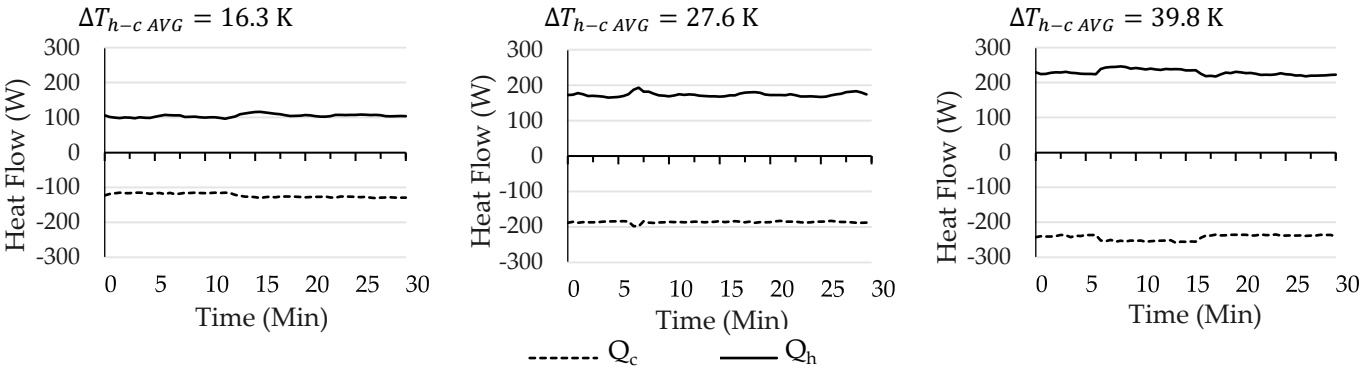

Figure 8. Heat flow in the cold and hot sides for the three tests performed.

The results depicted in Figure 8 demonstrate that the heat flow differs significantly across tests. Heat flow remains relatively stable, on average; however, fluctuations are observed due to slight variations in temperatures and flow rates. The average heat flow for the hot and cold sides was as follows in Table 4.

Table 4. Average heat flow and respective standard deviation for hot and cold sides across the three tests.

	Q_h [W]	σ_{Q_c} [W]	Q_c [W]	σ_{Q_c} [W]
Test 1 : $\Delta T_{h-c\ AVG} = 16.3$ K	−123.27	6.47	105.71	5.41
Test 2 : $\Delta T_{h-c\ AVG} = 27.6$ K	−187.94	4.69	174.14	6.82
Test 3 : $\Delta T_{h-c\ AVG} = 39.8$ K	−244.03	9.65	230.24	9.70

These results point towards a heat transfer rate that is slightly higher on the hot side compared to the cold side. The low value of the temperature differentials ΔT_c and ΔT_h makes the impact of even minor sensor reading inaccuracies relatively significant.

From Table 4, the heat flow differences between the hot and cold sides are 17.6 W for Test 1, 13.8 W for Test 2, and 13.8 W for Test 3.

These values are acceptable and are attributed to the heat power extracted by the TEG and thermal losses to the surroundings, as the TEG HX system is not perfectly insulated.

3.4. Electric Power Generation

The power generated by the TEG during the tests is presented in Figure 8. The maximum generated power (P_{elec}) values of 0.20 W, 0.53 W, and 0.93 W were obtained for the respective tests with a resistance value (R) of 10.61 Ω. This graph illustrates the relation between the resistive load and power generation for the different temperature differentials and a relatively low electrical output of the TEG under the given experimental conditions. Though resistance values were tested up to 14,861.44 Ω, only power measurements with R values up to 149.82 Ω are presented in Figure 9. Beyond this threshold, power generation slowly tends to zero (P_{elec} values for R = 14,861.44 Ω were 0.00021 W, 0.00056 W, and 0.00101 W). Nonetheless, it is observed that as expected, for every resistance value, power increases with temperature difference, highlighting the TEG's capability to convert temperature differentials into electrical energy.

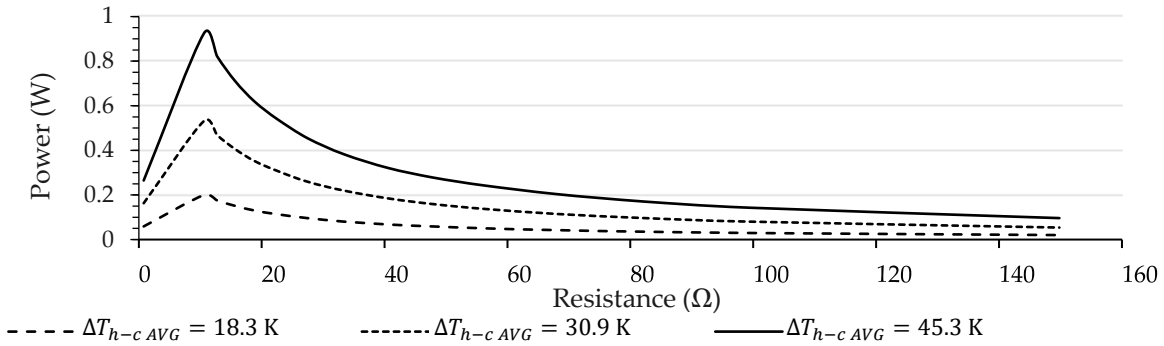

Figure 9. Electric power generated using the TEG module for resistance values between 0.78 Ω and 149.82 Ω for each of the three tests performed.

When comparing the power involved in heat transfer with the power generated by the TEG, we observe a significant difference in their magnitudes, as shown in Table 5.

Table 5. Maximum values of P_{elec} across the three $\Delta T_{h-c\ AVG}$ tests.

	$R_{P_{elecmax}}$ [Ω]	$P_{elecmax}$ [W]
Test 1: $\Delta T_{In\ h-c\ AVG} = 16.3$ K	10.61	0.20
Test 2: $\Delta T_{In\ h-c\ AVG} = 27.6$ K	10.61	0.53
Test 3: $\Delta T_{In\ h-c\ AVG} = 39.8$ K	10.61	0.93

The heat flow difference between the hot and cold sources ranged from 13.8 W to 17.6 W, and the TEG power ranged from 0.20 W to 0.93 W. This indicates that the TEG power is approximately two orders of magnitude smaller than the average heat rate between the hot and cold heat sources. Although this effect can be mitigated by implementing methods to reduce heat losses and seeking more efficient TEG modules, the purpose of this study is not to find an efficient method for energy production. Instead, the aim is to develop a method for powering a sensor in remote locations where a temperature differential already exists.

4. Discussion

The system detailed in Section 2 requires energy for six measurements and one transmission per hour, with the remaining time in a low-power sleep mode. This was calculated to require a total energy of 13.5 J per hour.

With this requirement in mind, and with results from the testing of the TEG HX, it is now possible to assess whether this system can generate sufficient energy. Using the P_{elec} values obtained from Table 5, it is possible to determine the energy generated over a period of one hour using Equation (11). These calculations were performed, and the results are compiled in Table 6.

Table 6. Energy generated over the period of one hour using the different tested conditions.

	Energy [J]
Test 1 : $\Delta T_{In\ h-c\ AVG} = 16.3$ K	720.0
Test 2 : $\Delta T_{In\ h-c\ AVG} = 27.6$ K	1914.5
Test 3 : $\Delta T_{In\ h-c\ AVG} = 39.8$ K	3330.4

The energy generated by the TEG HX under the different tested conditions increases with the temperature differential. Even in the lowest temperature differential scenario (Test 1), the energy generated (720.0 J) by far exceeds the minimum energy requirement (13.5 J) necessary to power the frost-measuring sensor system. As the temperature differential increases, the energy generation substantially surpasses the required power to maintain the active sensing system and transmits data without the need to return to deep sleep, with Test 2 generating 1914.5 J and Test 3 generating 3330.4 J.

The tests were conducted using a TEG HX composed of four Peltier modules, each with an area of 50 × 50 mm. The findings indicate that a single Peltier module can generate 180.0 J of energy under the conditions of Test 1, 478.6 J under Test 2 conditions, and 832.6 J under Test 3 conditions. These values significantly exceed the minimum energy requirement of 13.5 J calculated in Section 2. Based on the Peltier cell area (50 × 50 mm), the minimum required area per device can be calculated: 13.7 × 13.7 mm for Test 1, 8.4 × 8.4 mm for Test 2, and 6.4 × 6.4 mm for Test 3.

These calculations do not account for potential losses, irregularities, standard size availability, or variations in module efficiency. Thus, the actual required size would likely be larger. However, these estimates provide an indication of the potential for system miniaturization. This miniaturization is important, as the implementation of a TEG HX will add thermal resistance in the place where heat exchange is desired, which might be problematic. Nevertheless, a sensor with a TEG HX and a small footprint could have a negligible impact on a larger system.

These findings indicate that the TEG HX can generate sufficient energy to power the frost-measuring sensor system under the tested conditions. This supports the feasibility of using TEG for continuous operation of the system, assuming that potential losses in energy accumulation and transmission are adequately managed. The surplus energy generated, particularly in higher temperature differential scenarios, also provides a buffer to account for any inefficiencies or additional energy needs associated with higher transmission or measurement frequencies that may arise.

Though the TEG HX can generate sufficient energy to power the frost-measuring sensor system, it is important to note that this method is inherently inefficient. The TEG process captures only a very small fraction of the energy, with the majority being dissipated. This makes this method of powering the frost-measuring sensors viable only if the primary goal of the system is heat transfer, and the generation of electrical energy is a secondary benefit. In such cases, the TEG HX can be placed within the system to harness a minute portion of the heat, converting it into electrical energy to power low-energy devices, such as sensors, without significantly impacting the primary heat transfer function of the heat exchanger.

5. Conclusions

The current study aims to evaluate the feasibility of using thermoelectric energy harvesting to power frost detection sensors in refrigeration systems. An experimental setup was developed to simulate the conditions found in refrigeration units, with a TEG HX module containing four Peltier cells. One side of the module was refrigerated, and the other was heated, representing a temperature gradient where heat conduction is observed. The primary objective was to measure the power output of the TEG HX and assess its potential for remote sensor applications. The ability to convert heat flow into electrical energy for powering frost detection sensors presents a dual potential for energy efficiency. On the one hand, the sensor contributes to accurate frost detection and demand defrosting operations. On the other hand, the power for this system can be obtained from the dissipation of waste heat, such as in the condenser, by extracting energy from a temperature gradient that the refrigeration system creates to discard the heat. If waste heat is not available, a small amount of energy can be obtained from a location where heat flow is already desired, at the expense of introducing a small amount of heat resistance to the HX. In such cases, the system should be designed to minimize disruption to normal system parameters, either by having a small footprint or by being placed in a way such that its thermal resistance does not significantly impact the normal heat exchange process.

The TEG HX system developed in this work proved capable of producing enough energy to power the frost-measuring sensor, with generated energy in all tested conditions exceeding the minimum required 13.5 J per hour. Even under the smallest temperature differential, the energy output was above the necessary threshold, showcasing the system's potential effectiveness across different scenarios.

The footprint reduction is therefore achievable, as the studied TEG HX module can be minimized to areas as small as 13.7 $\times$ 13.7 mm based on the results of Test 1, 8.4 $\times$ 8.4 mm based on Test 2, and 6.4 $\times$ 6.4 mm based on Test 3, reducing the impact on overall system efficiency.

Despite its capability to generate sufficient electrical energy, this system is inefficient for electrical energy production compared to the amount of energy involved. This approach is practical only in scenarios where heat exchange is already occurring, and generating electrical energy is a secondary objective, such as when placing a TEG between the evaporator and intake air, between the condenser and refrigerating air, or in the liquid-to-suction line used to superheat the gas and subcool the liquid, as demonstrated by Attar et al. [20]. This approach ensures that the TEG generates electrical power without adding undesired thermal loads to the refrigeration system, which would otherwise have a negative impact surpassing any positive contribution brought by the frost-measuring sensor.

Future works will focus on increasing efficiency, reducing the system footprint, and finding more efficient Peltier modules, as studies by other authors have demonstrated higher energy generation, albeit still low.

Energy storage and voltage regulation must also be developed for the practical application of this system.

Author Contributions: Conceptualization, M.L.d.A. and P.D.d.S.; methodology, M.L.d.A., P.D.G. and P.D.d.S.; software, M.L.d.A.; validation, P.D.d.S.; formal analysis, M.L.d.A., P.D.G. and P.D.d.S.; investigation, M.L.d.A., P.D.G. and P.D.d.S.; resources, P.D.G.; data curation, M.L.d.A.; writing—

original draft preparation, M.L.d.A.; writing—review and editing, P.D.G. and P.D.d.S.; supervision, P.D.d.S.; funding acquisition, P.D.G. All authors have read and agreed to the published version of the manuscript.

Funding: This work was supported by the Portuguese Foundation for Science and Technology, I.P. (FCT, I.P.) FCT/MCTES through national funds (PIDDAC), under the R&D Unit C-MAST - Center for Mechanical and Aerospace Science and Technologies, with reference projects UIDB/00151/2020 and UIDP/00151/2020, https://doi.org/10.54499/UIDB/00151/2020 and https://doi.org/10.54499/UIDP/00151/2020, respectively.

Data Availability Statement: Data is available upon request.

Conflicts of Interest: The authors declare no conflicts of interest.

References

1. Wang, W.; Feng, Y.C.; Zhu, J.H.; Li, L.T.; Guo, Q.C.; Lu, W.P. Performances of Air Source Heat Pump System for a Kind of Mal-Defrost Phenomenon Appearing in Moderate Climate Conditions. *Appl. Energy* **2013**, *112*, 1138–1145. [CrossRef]
2. Hermes, C.J.; Silva, D.L.; Melo, C. Experimental study of frost accumulation on fan-supplied tube-fin evaporators. *Appl. Therm. Eng.* **2011**, *31*, 1013–1020. [CrossRef]
3. Heidinger, G.G.; Nascimento, S.M.; Gaspar, P.D.; Silva, P.D. Experimental study of the fins arrangement pattern of refrigerated display cabinet evaporator towards thermal performance improvement. *Appl. Therm. Eng.* **2018**, *138*, 246–253. [CrossRef]
4. Gaspar, P.D.; Gonçalves, L.C.C.; Pitarma, R.A. CFD parametric studies for global performance improvement of open refrigerated display cabinets. *Model. Simul. Eng.* **2012**, *2012*, 867820. [CrossRef]
5. Gaspar, P.D.; Gonçalves, L.C.C.; Pitarma, R.A. Three-Dimensional CFD modelling and analysis of the thermal entrainment in open refrigerated display cabinets. In Proceedings of the ASME 2008 Heat Transfer Summer Conference (HT 2008), Jacksonville, FL, USA, 10–14 August 2008; Volume 2, pp. 63–73. [CrossRef]
6. Gaspar, P.D.; Silva, P.D.; Nunes, J.; Andrade, L.P. Characterization of the specific electrical energy consumption of agrifood industries in the central region of Portugal. *Appl. Mech. Mater.* **2014**, *590*, 878–882. [CrossRef]
7. Silva, P.D.; Gaspar, P.D.; Nunes, J.; Andrade, L.P.A. Specific electrical energy consumption and CO_2 emissions assessment of agrifood industries in the central region of Portugal. *Appl. Mech. Mater.* **2014**, *675–677*, 1880–1886. [CrossRef]
8. Nunes, J.; Silva, P.D.; Andrade, L.P.; Gaspar, P.D. Characterization of the specific energy consumption of electricity in the Portuguese sausage industry. *WIT Trans. Ecol. Environ.* **2014**, *186*, 763–774. [CrossRef]
9. Aguiar, M.L.; Gaspar, P.D.; Silva, P.D. Image recognition method for frost sensing applications. *Energy Rep.* **2022**, *8*, 234–240. [CrossRef]
10. Hermes, C.J.L.; Boeng, J.; da Silva, D.L.; Knabben, F.T.; Sommers, A.D. Evaporator frosting in refrigerating appliances: Fundamentals and applications. *Energies* **2021**, *14*, 5991. [CrossRef]
11. Aguiar, M.L.; Gaspar, P.D.; Silva, P.D.; Silva, A.P.; Martinez, A.M. Medium materials for improving frost detection on a resistive sensor. *Energy Rep.* **2020**, *6*, 263–269. [CrossRef]
12. Aguiar, M.; Gaspar, P.D.; Silva, P.D. Optimized Placement of Frost-Measuring Sensors in Heat Exchangers via Image Processing of Frost Formation Pattern. *Sensors* **2023**, *23*, 5253. [CrossRef] [PubMed]
13. Ge, Y.; Sun, Y.; Wang, W.; Zhu, J.; Li, L.; Liu, J. Field test study of a novel defrosting control method for air-source heat pumps by applying tube encircled photoelectric sensor. *Int. J. Refrig.* **2016**, *66*, 133–144. [CrossRef]
14. Shen, Y.; Wang, S. Condensation frosting detection and characterization using a capacitance sensing approach. *Int. J. Heat Mass Transf.* **2020**, *147*, 118968. [CrossRef]
15. Aguiar, M.L.; Gaspar, P.D.; Silva, P.D. Frost measurement sensors for demand defrost control systems: Purposed applications in evaporators. In *Transactions on Engineering Technologies*; Ao, S.I., Gelman, L., Kim, H., Eds.; WCE 2018; Springer: Singapore, 2019; Chapter 12; pp. 159–171, ISBN 978-981-32-9530-8. [CrossRef]
16. Gubbi, J.; Buyya, R.; Marusic, S.; Palaniswami, M. Internet of Things (IoT): A vision, architectural elements, and future directions. *Future Gener. Comput. Syst.* **2013**, *29*, 1645–1660. [CrossRef]
17. Di Meglio, A.; Massarotti, N.; Nithiarasu, P. A physics-driven and machine learning-based digital twinning approach to transient thermal systems. *Int. J. Numer. Methods Heat Fluid Flow* **2006**. [CrossRef]
18. Rowe, D.M. *Thermoelectrics Handbook: Macro to Nano*; CRC Press: Boca Raton, FL, USA, 2006. [CrossRef]
19. Alvarez-Quintana, J. Energy production through residual heat harvesting from domestic/commercial fridges using nanostructured thermoelectric modules. *Therm. Sci. Eng. Prog.* **2023**, *42*, 101952. [CrossRef]
20. Attar, A.; Rady, M.; Abuhabaya, A.; Albatati, F.; Hegab, A.; Almatrafi, E. Performance Assessment of Using Thermoelectric Generators for Waste Heat Recovery from Vapor Compression Refrigeration Systems. *Energies* **2021**, *14*, 8192. [CrossRef]

21. Espressif Systems. ESP32 Series Datasheet. *Version 4.5*. 2024. Available online: https://www.espressif.com/documentation/esp32_datasheet_en.pdf (accessed on 5 June 2023).
22. Kuang, Y.; Ruan, T.; Chew, Z.J.; Zhu, M. Energy harvesting during human walking to power a wireless sensor node. *Sens. Actuators A Phys.* **2017**, *254*, 69–77. [CrossRef]

Disclaimer/Publisher's Note: The statements, opinions and data contained in all publications are solely those of the individual author(s) and contributor(s) and not of MDPI and/or the editor(s). MDPI and/or the editor(s) disclaim responsibility for any injury to people or property resulting from any ideas, methods, instructions or products referred to in the content.